ACS APPLIED MATERIALS & INTERFACES

Research Article

www.acsami.org

Highly Dispersed CeO_2 on TiO_2 Nanotube: A Synergistic Nanocomposite with Superior Peroxidase-Like Activity

Hui Zhao, Yuming Dong,* Pingping Jiang,* Guangli Wang, and Jingjing Zhang

Key Laboratory of Food Colloids and Biotechnology (Ministry of Education of China), School of Chemical and Material Engineering, Jiangnan University, Wuxi, Jiangsu 214122, P. R. China

Supporting Information

ABSTRACT: In this report, a novel nanocomposite of highly dispersed CeO_2 on a TiO_2 nanotube was designed and proposed as a peroxidase-like mimic. The best peroxidase-like activity was obtained for the CeO_2/nanotube-TiO_2 when the molar ratio of Ce/Ti was 0.1, which was much higher than that for CeO_2/nanowire-TiO_2, CeO_2/nanorod-TiO_2, or CeO_2/nanoparticle-TiO_2 with a similar molar ratio of Ce/Ti. Moreover, in comparison with other nanomaterial based peroxidase mimics, CeO_2/nanotube-TiO_2 nanocomposites exhibited higher affinity to H_2O_2 and 3,3′,5,5′-tetramethylbenzidine (TMB). Kinetic analysis indicated that the catalytic behavior was in accordance with typical Michaelis−Menten kinetics. Ce^{3+} sites were confirmed as the catalytic active sites for the catalytic reaction. The first interaction of surface CeO_2 with H_2O_2 chemically changed the surface state of CeO_2 by transforming Ce^{3+} sites into surface peroxide species causing adsorbed TMB oxidation. Compared with CeO_2/nanowire-TiO_2, CeO_2/nanorod-TiO_2, and CeO_2/nanoparticle-TiO_2, the combination of TiO_2 nanotube with CeO_2 presented the highest concentration of Ce^{3+} thus leading to the best peroxidase-like activity. On the basis of the high activity of CeO_2/nanotube-TiO_2, the reaction provides a simple method for colorimetric detection of H_2O_2 and glucose with the detection limits of 3.2 and 6.1 μM, respectively.

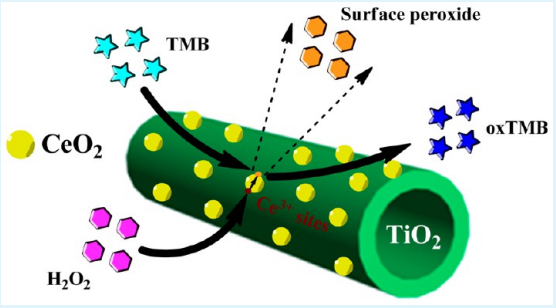

KEYWORDS: *CeO_2/TiO_2 nanocomposite, peroxidase mimic, synergistic effect, H_2O_2, glucose*

INTRODUCTION

Owing to their high substrate specificity and efficiency under mild reaction conditions, natural enzymes have been widely studied and applied in biosensing, pharmaceutical processes, the food industry, agrochemical production, etc.[1,2] However, they bear some drawbacks, such as the sensitivity of catalytic activity to environmental changes and low operational stability due to denaturation and digestion, as well as the high costs in preparation and purification.[1−4] A solution to these limitations can be provided by the rapid growth of the nanotechnology field, from which nanostructural materials have emerged as enzyme mimics due to their high surface energies and large surface-to-volume ratios. In comparison with natural enzymes, nanomaterial based enzyme mimics exhibit a high stability against harsh reaction conditions. Meanwhile, they possess additional advantages of controlled preparation at low cost, flexibility in structure design and composition, and tunable catalytic activities. To date, there have been many works on exploiting inorganic nanostructured materials as peroxidase mimics.[5−12]

Among the countless examples of the nanomaterial based enzyme mimics, in order to achieve highly active nanomaterial based enzyme mimics, a new generation of composite nanomaterials with well-defined structures is particularly impressive and offers great opportunities for catalysis which takes one of the most pivotal steps toward enzyme mimicry. Nanocomposites have been proposed to realize the combination of the respective properties of each component or to achieve cooperatively enhanced performances. A variety of nanocomposites with inorganic nanomaterials incorporated with the nanoscale matrixes with a large specific surface area have been applied as enzyme mimics. Typically, gold nanoparticles/gold nanoclusters/Au−Pd bimetallic nanoparticles−graphene hybrids[13−16] and a gold nanoparticles−carbon nanotube nanocomplex[17] were exploited with peroxidase-like catalytic activity. However, their practical applications are highly limited due to high cost of noble metal. It is known that many low-cost and common metal oxide nanostructures, such as Fe_3O_4 nanoparticles,[18] Co_3O_4 nanoparticles,[19] CuO nanoclusters,[20] and V_2O_5 nanowires,[21] have been proven to be the effective artificial peroxidase mimics. In addition, the preparation of metal oxide nanomaterials becomes controllable, and the lattice matching between metal oxides is easy to realize. Recently, much research interest has been directed toward metal oxide based composite nanomaterials. The combination of metal oxides and the special structural characteristic of composite could make their performance different from any one of the pure metal oxides. Up to now, according to our

Received: October 16, 2014
Accepted: March 16, 2015
Published: March 16, 2015

DOI: 10.1021/acsami.5b00023
ACS Appl. Mater. Interfaces 2015, 7, 6451−6461

knowledge, the metal oxide composite nanomaterial on the metal oxide support is much less studied. The effective combination of metal oxides and the strong interaction of metal oxides can make metal oxide supported metal oxide composite nanomaterial a promising enzyme mimic. Therefore, the discovery and development of new enzyme mimics that are composed of inexpensive metal oxide composites are highly desirable.

CeO_2 is an important rare earth metal oxide. Due to the low energy cost for the formation of extremely catalytic active oxygen vacancies and Ce^{3+} centers,[22] CeO_2 has been used as an efficient catalyst itself or a subtle structural and electronic promoter in various chemical processes.[23−26] Particularly, in biomimetic catalytic applications, besides possessing the high biocompatibility, CeO_2 is capable of mimicking the activity of several natural redox enzymes which is largely based on the $Ce^{4+} \leftrightarrow Ce^{3+}$ redox switch.[27−32] In order to effectively manipulate the Ce^{4+}/Ce^{3+} ratio, the introduction of other metal oxides has been developed as a feasible strategy.[33−35] Titanium is the second most abundant transition metal in the Earth's crust. Titanium oxide, TiO_2, has attractive properties including low cost, nontoxicity, and high stability. In the reported case of CeO_2−TiO_2 systems, it has been demonstrated theoretically and experimentally that Ce^{3+} sites could be effectively stabilized by the interfacial hybridization with TiO_2 support because of the energy decrease of the Ce 4f levels as a result of the mixing with the O 2p band of TiO_2.[36,37] Therefore, the combination of CeO_2 and TiO_2 will be attractive to construct an efficient metal oxide−metal oxide enzyme mimic. More recently, TiO_2@CeO_x core−shell nanoparticles have been reported as artificial enzymes with peroxidase-like activity which is tailored by CeO_2 shell thickness.[38] Therefore, it is deduced that different TiO_2 supports maybe potentially affect the peroxidase-like activity of CeO_2−TiO_2. Recently, the TiO_2 nanotube has been found to be a promising support because of its special structural characteristics and physicochemical properties.[39−42] In light of the superiority of the TiO_2 nanotube, the TiO_2 nanotube and CeO_2 nanoparticle were thus integrated into nanocomposites and developed as novel and efficient peroxidase mimics in this work. For comparison, various CeO_2/TiO_2 nanocomposites were prepared on the basis of TiO_2 nanowires, nanorods, and nanoparticle supports, respectively. Their structural characteristics and catalytic performances are evaluated. Reactive kinetics and mechanisms are investigated and discussed in detail. Additionally, we develop a new facile colorimetric method for H_2O_2 and glucose detection with the CeO_2/nanotube-TiO_2 composite as a peroxidase mimic.

EXPERIMENTAL SECTION

Preparation. TiO_2 nanotubes were synthesized by a hydrothermal approach, which has been described in detail elsewhere.[43,44] In brief, 5 g of TiO_2 powder (Sinopharm Chemical Reagent Co., Ltd.) was dispersed in 70 mL of 10 M NaOH and then transferred into a 100 mL Teflon-lined autoclave container. The autoclave was maintained at 140 °C under autogenous pressure for 20 h. The precipitated powder was filtered and washed with 0.1 M HNO_3 and deionized water for several times until the pH value of the rinsing solution became neutral, followed by being air-dried at 105 °C. The resulting product was denoted as NT-TiO_2.

CeO_2/NT-TiO_2 nanocomposites were prepared by a wet-chemical deposition precipitation method. The preparation procedure is as follows. Various amounts of $Ce(NO_3)_3 \cdot 6H_2O$ were dissolved in 50 mL of distilled water and mixed with 0.01 mol of NT-TiO_2, and sufficient $NH_3 \cdot H_2O$ (wt %: 25%−28%) was then added under vigorous stirring to adjust the pH to about 10. After that, this mixture was stirred again for 2 h and then aged for 4 h at room temperature to facilitate the formation of dispersed cerium species on the TiO_2 surface. The resulting product was dried at 105 °C for 12 h before being annealed at 400 °C for 2 h to generate CeO_2/NT-TiO_2. The prepared nanocomposites were designated as CeO_2/NT-TiO_2@X, where X referred to the molar ratio value of Ce/Ti. CeO_2 nanoparticles, labeled as NP-CeO_2, were obtained when there was no NT-TiO_2 added.

For comparison, the different CeO_2/TiO_2 nanocomposites based on TiO_2 nanowires, nanorods, and nanoparticles were prepared by the same wet-chemical deposition precipitation method, which were marked as CeO_2/NW-TiO_2, CeO_2/NR-TiO_2, and CeO_2/NP-TiO_2, respectively. The preparation procedure of TiO_2 nanowire (NW-TiO_2) was nearly similar to that of NT-TiO_2, but the higher hydrothermal temperature of 200 °C was indispensable.[43,44] In order to obtain the TiO_2 nanorod (NR-TiO_2) and TiO_2 nanoparticle (NP-TiO_2), the prepared NT-TiO_2 was annealed at 450 and 550 °C for 2 h, respectively.

Characterization. X-ray diffraction (XRD) patterns were recorded on an D8 X-ray diffractometer (Bruker AXS, German) at 40 kV and 40 mA using Cu Kα radiation (λ = 1.5406 Å). Transmission electron microscopy (TEM) and scanning electron microscopy (SEM) images were collected on a JEM-2100 (JEOL, Japan) transmission electron microscope at an accelerating voltage of 200 kV and an S-4800 (Hitachi, Japan) scanning electron microscope at an accelerating voltage of 3 kV, respectively. Energy-dispersive X-ray spectroscopy (EDX) was taken on the TEM. The Brunauer-Emmet-Teller (BET) surface area, total pore volume, and average pore sizes of sample were measured on an ASAP 2020 instrument (Micromeritics, USA) at liquid nitrogen temperature (77 K). Before measurement, the sample was degassed under vacuum condition at 200 °C for 2 h. X-ray photoelectron spectroscopy (XPS) analysis was conducted using an ESCALAB 250 Xi (Thermo, USA) X-ray photoelectron spectrometer with Al Kα line as the excitation source (hν = 1484.6 eV). Raman spectra were recorded on a confocal microscopic Raman spectrometer (Renishow In-Via, USA) with a 785 nm laser light irradiation from 100 to 1100 cm^{-1} at a duration time of 10 s. Before analysis, the samples with and without H_2O_2 treatment were pressed into slices. UV−vis absorption spectra were recorded on a TU-1901 spectrophotometer (Beijing Purkinje General, China) with a 0.5 cm UV cell. Fluorescence spectra of 2-hydroxyterephthalic acid were measured on a Cary Esclipse fluorescence spectrophotometer.

Assay for Catalytic Activity Study and Glucose Detection. The catalytic reaction was performed at 25 °C using 50 μg/mL CeO_2, TiO_2, or CeO_2/TiO_2 in a reaction volume of 4 mL of acetate buffer (50 mM, pH 4.0) with 250 μM 3,3′,5,5′-tetramethylbenzidine (TMB) as substrate and 1 mM H_2O_2, unless otherwise stated. The absorbance at 652 nm after 10 min or the time-dependent absorbance changes at 652 nm within 10 min were examined. The kinetic analysis of CeO_2/TN-TiO_2@0.1 with TMB as substrate was performed using 50 μg of CeO_2/TN-TiO_2@0.1 with fixed concentration of H_2O_2 (1 mM) and varying concentrations of TMB (0, 50, 100, 150, 200, 250, and 300 μM). Similarly, the kinetic analysis with H_2O_2 as the substrate was performed using 50 μg of CeO_2/TN-TiO_2@0.1 with fixed concentration of TMB (250 μM) and varying concentration of H_2O_2 (0, 0.005, 0.01, 0.02, 0.05, 0.1, and 1 mM). Apparent kinetic parameters were calculated using Lineweaver−Burk plots of the double reciprocal of the Michaelis−Menten equation, $1/V = K_m/V_m(1/[S] + 1/K_m)$, where V is the initial velocity, V_m represents the maximal reaction velocity, $[S]$ corresponds to the concentration of substrate, and K_m is the Michaelis constant.

Glucose detection was carried out as follows: First, 100 μL of GO_x (5 mg/mL) in NaH_2PO_4 buffer (10 mM, pH 7.0) and 200 μL of D-glucose with various concentrations in NaH_2PO_4 buffer (10 mM, pH 7.0) were mixed and incubated at 37 °C for 30 min. Second, 400 μL of TMB (5 mM, ethanol solution), 100 μL of CeO_2/NT-TiO_2 stock solution (2.5 mg/mL), and 3200 μL of acetate buffer (0.2 M, pH 4.0) were successively added to the glucose reaction solution. Finally, the

DOI: 10.1021/acsami.5b00023
ACS Appl. Mater. Interfaces 2015, 7, 6451−6461

mixed solution was incubated at 25 °C for 10 min for standard curve measurement.

RESULTS AND DISCUSSION

Structure Characterization. Figure 1 showed the XRD patterns of TiO_2, CeO_2, and CeO_2/NT-TiO_2 with different Ce/Ti molar ratios. For the prepared TiO_2 (Figure 1a) and CeO_2 (Figure 1i), the characteristic peaks at 2θ = 25.4°, 37.8°, 48.5°, 54.2°, 55.4°, and 63.0° and 2θ = 28.5°, 33.1°, 47.5°, 56.3°, 59.1°, and 69.4° were attributable to the anatase phase of TiO_2 (JCPDS: 02-0406) and the cubic fluorite structure of CeO_2 (JCPDS: 81-0792), respectively. CeO_2/NT-TiO_2 showed a decreasing peak intensity of TiO_2 with the increasing CeO_2 loadings (Figure 1b–i). When the Ce/Ti molar ratio is raised over 0.1 (Figure 1e–i), the reflection peaks of CeO_2 were clearly found and enhanced with the further increase of CeO_2 loadings. When the Ce/Ti molar ratio was below 0.1, no obvious CeO_2 diffraction peaks were observed from XRD patterns possibly due to the low content of CeO_2 and the well dispersed CeO_2 particles on TiO_2 nanotube surface.

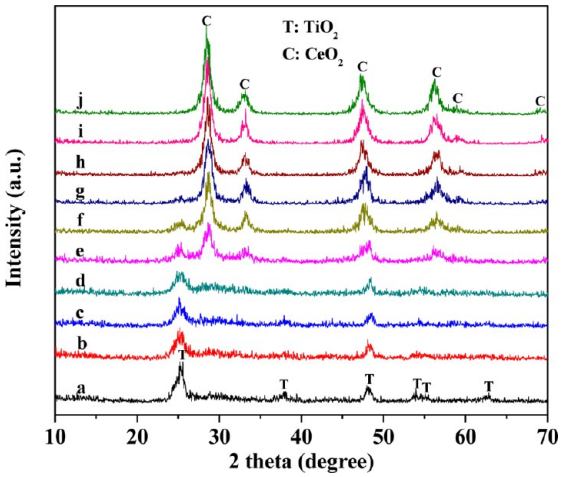

Figure 1. XRD patterns of TiO_2, CeO_2, and CeO_2/NT-TiO_2 with different molar ratio. (a) NT-TiO_2; (b) CeO_2/NT-TiO_2@0.01; (c) CeO_2/NT-TiO_2@0.025; (d) CeO_2/NT-TiO_2@0.1; (e) CeO_2/NT-TiO_2@0.2; (f) CeO_2/NT-TiO_2@0.5; (g) CeO_2/NT-TiO_2@1; (h) CeO_2/NT-TiO_2@2; (i) CeO_2/NT-TiO_2@5; (j) NP-CeO_2.

Figure 2a–k presented the TEM images of TiO_2, CeO_2, and CeO_2/NT-TiO_2 with different Ce/Ti molar ratios. The TiO_2 nanotube structure (Figure 2a) and the aggregated morphology for CeO_2 (Figure 2l) were observed. The outer and inner diameters of these TiO_2 tubes were estimated to be ~10 and ~4 nm, respectively. For CeO_2/NT-TiO_2@0.01 (Figure 2b) and CeO_2/NT-TiO_2@0.025 (Figure 2c) with lower contents of CeO_2 loadings, there were some CeO_2 particles with a size of several nanometers (<5 nm) observed on the surface of TiO_2 nanotubes. When the Ce/Ti molar ratio was raised to 0.1 (Figure 2d), CeO_2 particles with a size of 5–10 nm were spread on the TiO_2 nanotube surface. However, we did not observe the aggregated CeO_2, indicating that the presence of the TiO_2 nanotube significantly increases the dispersion of CeO_2 on its surface. The HRTEM image of CeO_2/NT-TiO_2@0.1 (Figure 2e) showed two interplane distances of about 0.24 and 0.31 nm corresponding to the (001) plane of TiO_2 and the (111) plane of CeO_2, respectively. Figure 2f gave the EDX spectrum of CeO_2/NT-TiO_2@0.1. The Ti, Ce, and O were clearly observed, and the atomic ratio of (Ti + Ce)/O was about 1/2 indicating the CeO_2/TiO_2 composite structure. However, the measured atomic ratio of Ce/Ti was over the atomic ratio (0.1) of the starting reagents. This was mainly due to most CeO_2 particles loaded on the TiO_2 nanotube surface leading to more Ce being detected by EDX. With the further increase of CeO_2 loadings, CeO_2/NT-TiO_2 showed a gradual agglomeration of CeO_2 on the TiO_2 surface (Figure 2g–k). The morphologies of CeO_2/NT-TiO_2@2 (Figure 2j) and CeO_2/NT-TiO_2@5 (Figure 2k) were even nearly similar to that of pure CeO_2 due to the serious clustering of CeO_2 on the TiO_2 nanotube surface. In addition, the texture characteristics, including the BET surface area and pore volume, of TiO_2, CeO_2, and CeO_2/NT-TiO_2 with different Ce/Ti molar ratios were analyzed, and the results were summarized in Table 1. CeO_2 had a low BET surface area (53 m^2/g) and pore volume (0.21 cm^3/g) while NT-TiO_2 possessed a large BET surface area (215 m^2/g) and pore volume (0.995 cm^3/g). Compared with CeO_2, CeO_2/NT-TiO_2 presents a higher BET surface area and pore volume when the Ce/Ti molar ratio was raised but not over 1, though the decreasing BET surface area and pore volume are observed for CeO_2/NT-TiO_2 with the increase of CeO_2 loading. CeO_2/NT-TiO_2@2 and CeO_2/NT-TiO_2@5 almost presented the similar texture characteristics as pure CeO_2 because of their similarly serious agglomeration morphologies as shown.

CeO_2/NW-TiO_2@0.1, CeO_2/NR-TiO_2@0.1, and CeO_2/NP-TiO_2@0.1 nanocomposites were prepared by using TiO_2 nanowire, nanorod, and nanoparticle as support, which were confirmed by TEM and SEM images in Figure 3a–f. Similar to CeO_2/NT-TiO_2@0.1, CeO_2 nanoparticles formed on the surfaces of TiO_2 nanowire, nanorod, and nanopaticle in CeO_2/NW-TiO_2@0.1, CeO_2/NR-TiO_2@0.1, and CeO_2/NP-TiO_2@0.1 nanocomposites. The insets in Figure 3a–c presented the representative HRTEM micrographs of CeO_2/NW-TiO_2@0.1, CeO_2/NR-TiO_2@0.1, and CeO_2/NP-TiO_2@0.1. They all showed two interplane distances of about 0.24 and 0.31 nm which corresponded to the (001) plane of TiO_2 and the (111) plane of CeO_2, respectively. However, different from CeO_2/NT-TiO_2@0.1, CeO_2/NW-TiO_2@0.1, CeO_2/NR-TiO_2@0.1, and CeO_2/NP-TiO_2@0.1 all showed obvious XRD patterns of cubic CeO_2 structure (Figure 4). These results indicated the better dispersion of CeO_2 particles on the surface of the TiO_2 nanotube than that of the TiO_2 nanowire, nanorod, and nanoparticle. Meanwhile, in comparison with CeO_2/NW-TiO_2@0.1, CeO_2/NR-TiO_2@0.1, and CeO_2/NP-TiO_2@0.1, CeO_2/NT-TiO_2@0.1 showed the larger BET surface area (172 m^2/g) and pore volume (0.812 cm^3/g), as summarized in Table 1.

Peroxidase-Like Activity. To demonstrate the peroxidase-like activity of CeO_2/NT-TiO_2@0.1, catalytic oxidation of the chromogenic substrate TMB in the presence or absence of H_2O_2 was tested. The intensity of adsorption peak at 652 nm can be used to evaluate the peroxidase-like activity of the sample. As shown in Figure 5A-a, almost no absorption at 652 nm was observed in the TMB + H_2O_2 system without CeO_2/NT-TiO_2@0.1, while the CeO_2/NT-TiO_2@0.1 + TMB system showed negligible adsorption at 652 nm (Figure 5A-b) under experimental conditions. In contrast, the CeO_2/NT-TiO_2@0.1 + TMB + H_2O_2 system produced a strong adsorption at 652 nm (Figure 5A-c). These results supported that the CeO_2/NT-TiO_2@0.1 behaved like peroxidase toward typical peroxidase substrates such as TMB. Moreover, only weak adsorption was observed in the NP-CeO_2 + TMB + H_2O_2 system (Figure 5A-

DOI: 10.1021/acsami.5b00023
ACS Appl. Mater. Interfaces 2015, 7, 6451–6461

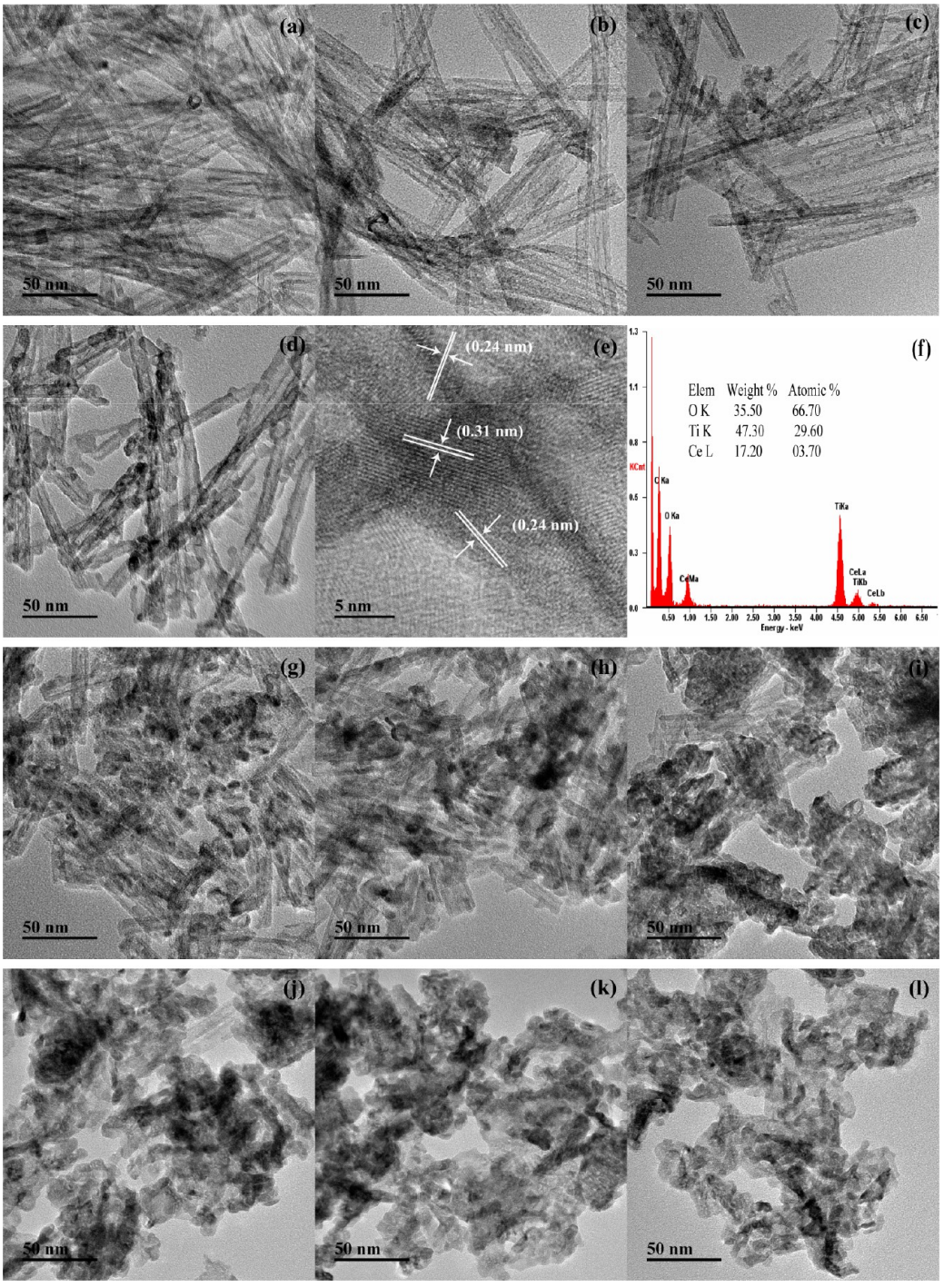

Figure 2. TEM images of TiO_2 (a), CeO_2 (l), and CeO_2/TiO_2 with different Ce/Ti molar ratios (a–d, g–l), as well as HRTEM image (e) and EDX spectrum (f) of CeO_2/NT-TiO_2@0.1, (b) CeO_2/NT-TiO_2@0.01; (c) CeO_2/NT-TiO_2@0.025; (d) CeO_2/NT-TiO_2@0.1; (g) CeO_2/NT-TiO_2@0.2; (h) CeO_2/NT-TiO_2@0.5; (i) CeO_2/NT-TiO_2@1; (j) CeO_2/NT-TiO_2@2; (k) CeO_2/NT-TiO_2@5.

d), and there was no adsorption at 652 nm for the NT-TiO_2 + TMB + H_2O_2 system (Figure 5A-e), indicating that the CeO_2 particles well dispersed on the NT-TiO_2 surface were responsible for the formation of the oxidation product of TMB in the CeO_2/NT-TiO_2@0.1 + TMB + H_2O_2 system. The inset showed the color variations of solutions in different reaction systems. When CeO_2/NT-TiO_2@0.1 was impregnated in TMB–acetate buffer solution for a certain time before adding H_2O_2 or the catalytic reaction was conducted under high TMB concentration, a significantly decreased catalytic efficiency was found (Figures S2 and S3, Supporting Information), which was because more TMB was adsorbed on the CeO_2/NT-TiO_2@0.1 surface inhibiting the reaction with H_2O_2. Additionally, the catalytic activity of CeO_2/NT-TiO_2@0.1 was enhanced with the increase of the H_2O_2 concentration (Figure S4, Supporting Information). Therefore, in catalytic oxidation of TMB with CeO_2/NT-TiO_2@0.1, the effective interaction of CeO_2/NT-TiO_2@0.1 with H_2O_2 was a critical step for TMB oxidation.

DOI: 10.1021/acsami.5b00023
ACS Appl. Mater. Interfaces 2015, 7, 6451–6461

Table 1. Texture Characteristics of TiO_2, CeO_2, and CeO_2/TiO_2

catalyst	BET surface area (m^2/g)	pore volume (cm^3/g)
NT-TiO_2	215	0.995
CeO_2/NT-TiO_2@0.01	212	0.989
CeO_2/NT-TiO_2@0.025	209	0.940
CeO_2/NT-TiO_2@0.1	178	0.812
CeO_2/NT-TiO_2@0.2	126	0.633
CeO_2/NT-TiO_2@0.5	98	0.358
CeO_2/NT-TiO_2@1	67	0.267
CeO_2/NT-TiO_2@2	58	0.246
CeO_2/NT-TiO_2@5	57	0.232
NP-CeO_2	53	0.231
CeO_2/NW-TiO_2@0.1	54	0.124
CeO_2/NR-TiO_2@0.1	91	0.540
CeO_2/NP-TiO_2@0.1	54	0.389

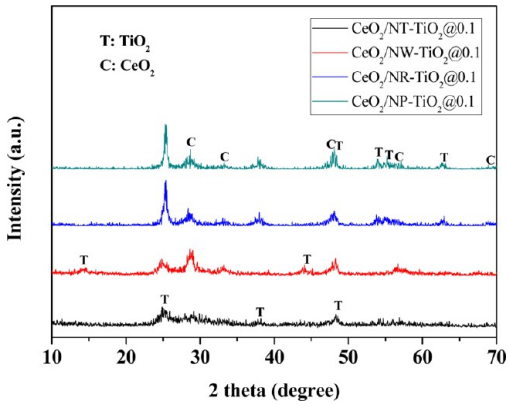

Figure 4. XRD patterns of CeO_2/TiO_2 with different TiO_2 morphologies.

The peroxidase-like activity of CeO_2/NT-TiO_2 with different Ce/Ti molar ratios was investigated (Figure 5B). With the increase of CeO_2 loadings, the peroxidase-like activity of CeO_2/NT-TiO_2 was initially enhanced. When the Ce/Ti molar ratio was raised to 0.1, the highest peroxidase-like activity was obtained for CeO_2/NT-TiO_2@0.1. However, with the further increase of CeO_2 loadings, CeO_2/NT-TiO_2 showed a decreasing peroxidase-like activity. In addition, compared with CeO_2/NW-TiO_2@0.1, CeO_2/NR-TiO_2@0.1, and CeO_2/NP-TiO_2@0.1, CeO_2/NT-TiO_2@0.1 showed the highest peroxidase-like activity (Figure 5C). Their abilities followed the order of CeO_2/NT-TiO_2@0.1 > CeO_2/NR-TiO_2@0.1 > CeO_2/NP-TiO_2@0.1 > CeO_2/NW-TiO_2@0.1.

Similar to peroxidase, the catalytic activity of CeO_2/NT-TiO_2@0.1 nanocomposites was dependent on pH and temperature. Influences of pH and temperature on the catalytic activity of CeO_2/NT-TiO_2@0.1 were studied (Figure S5, Supporting Information). The pH value varied from 2.6 to 8. The optimal pH was 4.0 for the maximum absorption. A temperature-dependent assay was also performed in this experiment. At a temperature from 15 to 75 °C, the absorbance at 652 nm first increased and then decreased after 45 °C. However, considering the convenience and economy of this catalytic process, the bioassay should be carried out at room temperature. Therefore, 25 °C was selected as the reaction temperature. To overcome the effect of possible leaching ions, the Ce and Ti ion contents of the supernatants were detected by AAS and the determined amount of Ce and Ti ions in the leaching solution is negligible. In addition, the catalytic activity of the Ce and Ti ions leached at pH 4.0 was tested as follows. The CeO_2/NT-TiO_2@0.1 nanocomposites were incubated with buffer at pH 4.0 for 10 min, and then, the supernatant solution without nanocomposites was used for the catalytic experiment. No absorbance at 652 nm (Figure S6, Supporting Information) further demonstrated that the catalytic effect did not come from leached ions but from CeO_2/NT-TiO_2@0.1.

Kinetics and Possible Reactive Mechanism. The kinetic parameters for the reaction were evaluated by the initial rate method with TMB and H_2O_2 as substrates. The absorbance

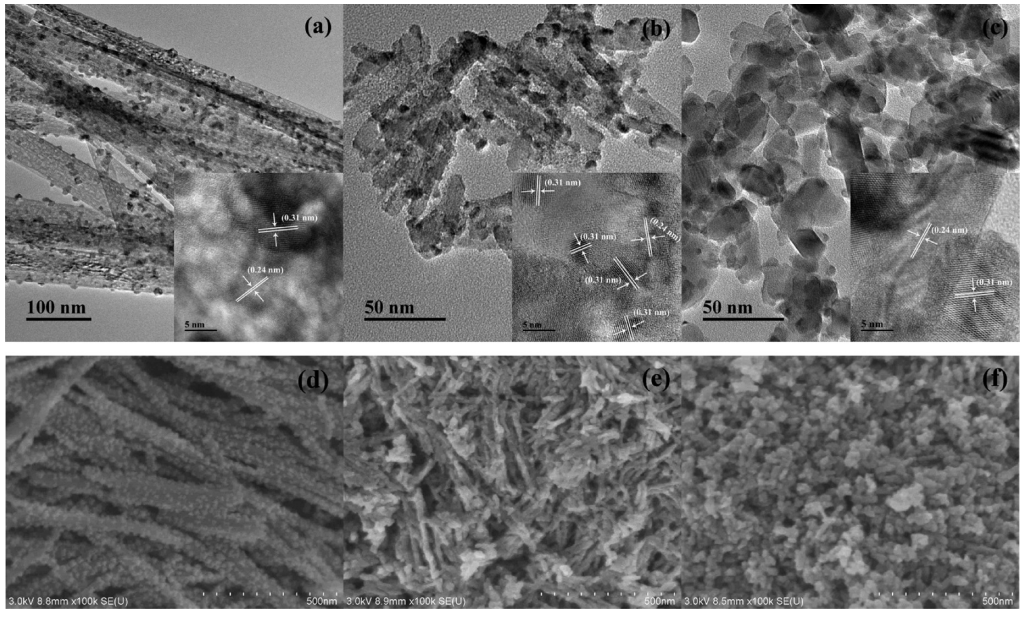

Figure 3. TEM (a–c) and SEM (d–f) images of CeO_2/TiO_2 nanocomposites with TiO_2 nanowire, nanorod, and nanoparticle as a support: (a, d) CeO_2/NW-TiO_2@0.1; (b, e) CeO_2/NR-TiO_2@0.1; (c, f) CeO_2/NP-TiO_2@0.1.

DOI: 10.1021/acsami.5b00023
ACS Appl. Mater. Interfaces 2015, 7, 6451–6461

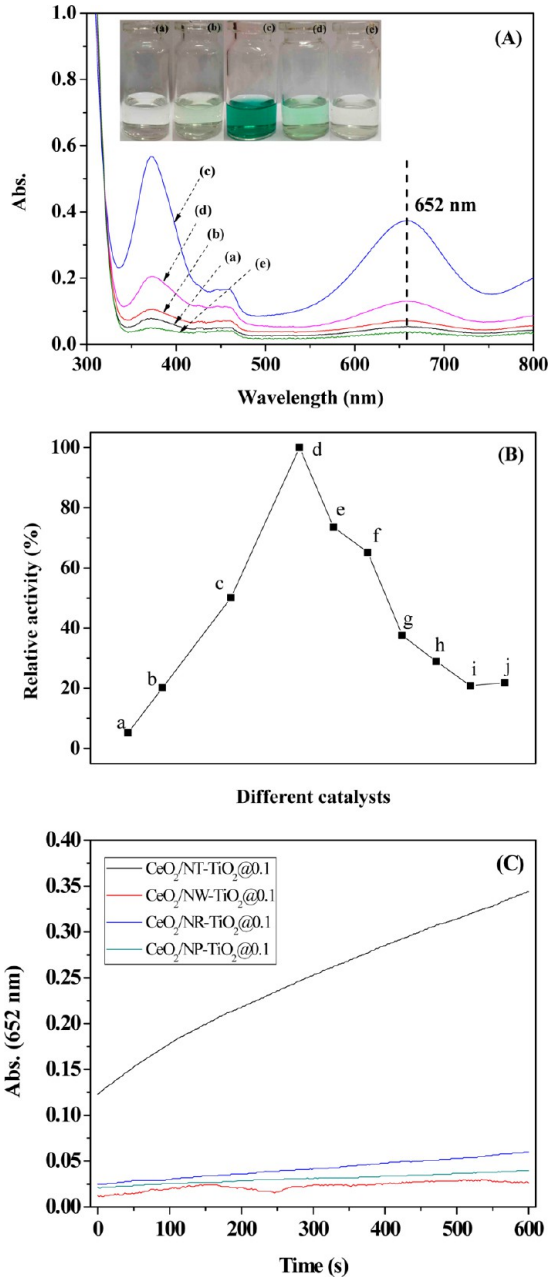

Figure 5. (A) UV−vis spectra at reaction time of 10 min in different systems; inset is the photograph of the solution at a reaction time of 10 min in different reaction systems. (a) TMB + H_2O_2, (b) TMB + CeO_2/NT-TiO_2@0.1, (c) TMB + H_2O_2 + CeO_2/NT-TiO_2@0.1, (d) TMB + H_2O_2 + NP-CeO_2, and (e) TMB + H_2O_2 + NT-TiO_2 in a pH 4.0 acetate buffer at 25 °C for 10 min. (B) Relative catalytic activity TiO_2, CeO_2, and CeO_2/TiO_2 with different Ce/Ti molar ratios. (a) NT-TiO_2, (b) CeO_2/NT-TiO_2@0.01, (c) CeO_2/NT-TiO_2@0.025, (d) CeO_2/NT-TiO_2@0.05, (e) CeO_2/NT-TiO_2@0.1, (f) CeO_2/NT-TiO_2@0.2, (g) CeO_2/NT-TiO_2@0.5, (h) CeO_2/NT-TiO_2@1, (i) CeO_2/NT-TiO_2@2, (j) CeO_2/NT-TiO_2@5, and (k) NP-CeO_2; the maximum point was set as 100%. (C) Time-dependent absorbance changes at 652 nm of TMB for CeO_2/NT-TiO_2@0.1, CeO_2/NW-TiO_2@0.1, CeO_2/NR-TiO_2@0.1, and CeO_2/NP-TiO_2@0.1 nanocomposites.

data were converted to the corresponding concentration term using the value ε = 39 000 $M^{-1}cm^{-1}$ (at 652 nm) for the oxidized product of TMB.[45] Within the suitable range of TMB (Figure 6a) and H_2O_2 (Figure 6b) concentrations, typical

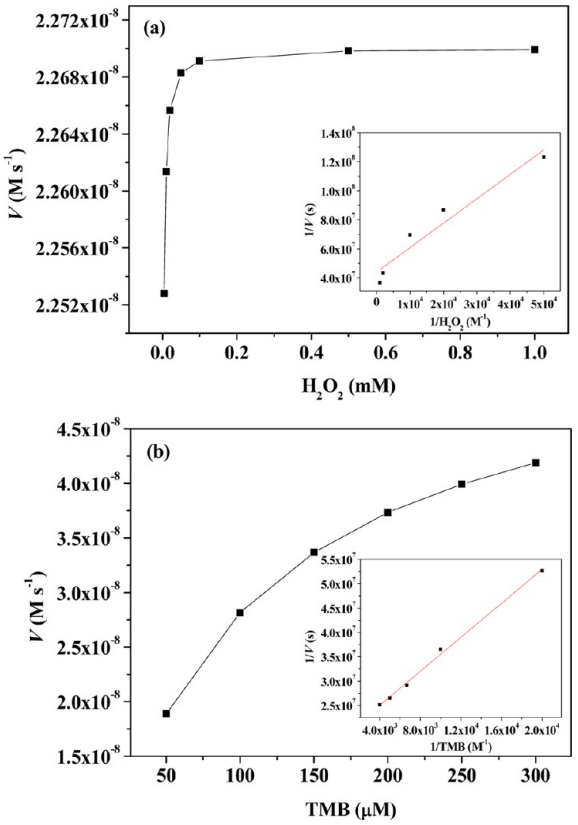

Figure 6. Steady-state kinetic analyses using the Michaelis−Menten model and Lineweaver−Burk model (insets) for CeO_2/NT-TiO_2@0.1 nanocomposite by (a) varying the concentration of TMB with a fixed amount of H_2O_2 and (b) varying the concentration of H_2O_2 with a fixed amount of TMB.

Michaelis−Menten curves were observed for CeO_2/NT-TiO_2@0.1 nanocomposites. The data were fitted to the Michaelis−Menten model to obtain the catalytic parameters K_m and V_m given in Table 2. All these parameters were also evaluated from the Lineweaver−Burk double-reciprocal plot,[46] which gave analogous values (Figure 6a,b insets). As an apparent Michaelis−Menten constant, the K_m value with TMB as substrate for CeO_2/NT-TiO_2@0.1 (0.097 mM) was lower than that of HRP (0.434 mM).[47] This result suggested that CeO_2/NT-TiO_2@0.1 had a higher affinity than that of HRP toward TMB. On the other hand, the K_m value of CeO_2/NT-TiO_2@0.1 with H_2O_2 as substrate was 0.04 mM, which was about 83.5 times lower than that of HRP, suggesting that a significantly lower H_2O_2 concentration was required for the nanocomposites than for HRP when maximum activity was obtained. Moreover, the K_m and V_m values of the CeO_2/NT-TiO_2@0.1 and other peroxidase mimics were compared, and the data was summarized in Table S1, Supporting Information. Evidently, the CeO_2/NT-TiO_2@0.1 had a much higher affinity to H_2O_2 and TMB than other mimics.

According to the previous studies on the bioapplication of cerium oxide as a peroxidase mimic,[28,30−32,38] it was prposed that the efficiency of CeO_2 artificial peroxidase-like enzyme strongly depended on the Ce^{4+}/Ce^{3+} ratio where the low Ce^{3+}/Ce^{4+} ratio was largely helpful. In order to evaluate the role of CeO_2 in prepared samples, high-resolution Ce 3d XPS spectra for pure CeO_2 (Figure S7, Supporting Information) and CeO_2/NT-TiO_2@0.1 were recorded (Figure 7). For pure CeO_2, the peaks at V_0, V′, U_0, and U′ (881.6, 884.7, 899.4, and 902.5 eV)

DOI: 10.1021/acsami.5b00023
ACS Appl. Mater. Interfaces 2015, 7, 6451−6461

Table 2. Comparison of the Apparent Michaelis-Menten Constant (K_m) and Maximum Reaction Rate (V_m)

catalyst	K_m (mM)		V_m (M s^{-1})		ref.
	TMB	H_2O_2	TMB	H_2O_2	
HRP	0.434	3.70	10.0×10^{-8}	8.71×10^{-8}	32
CeO_2/NT-TiO_2@0.1	0.097	0.04	5.54×10^{-8}	2.27×10^{-8}	this work

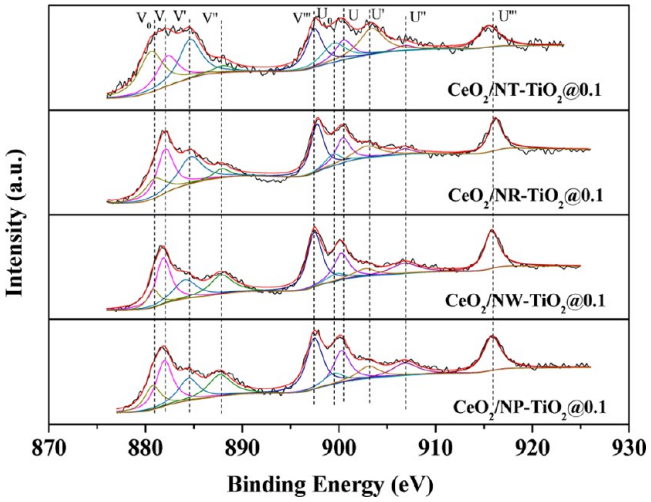

Figure 7. High-resolution of Ce 3d XPS spectra of CeO_2/NT-TiO_2@0.1, CeO_2/NR-TiO_2@0.1, CeO_2/NW-TiO_2@0.1, and CeO_2/NP-TiO_2@0.1.

represented the presence of Ce^{3+} while characteristic peaks of Ce^{4+} presented at V, V″, V‴, U, U″, and U‴ (882.9, 888.9, 897.9, 900.9, 907.2, and 916.2 eV).[38,48,49] In comparison with those of pure CeO_2, the characteristic peaks of Ce 3d in CeO_2/TiO_2@0.1 shifted to lower binding energy positions, which is due to the different types of screening that TiO_2 (band gap 3 eV) and CeO_2 (band gap 6 eV) can provide in the final state of the photoemission process or most probably to the presence of band bending in CeO_2/TiO_2@0.1.[37] The calculated concentrations of Ce^{3+} were 28.1%, 57.6%, 36.3%, 31.2%, and 29.8% in pure CeO_2, CeO_2/NT-TiO_2@0.1, CeO_2/NR-TiO_2@0.1, CeO_2/NP-TiO_2@0.1, and CeO_2/NW-TiO_2@0.1 (Table 3), respectively. Clearly, in our work, the presence of TiO_2 supports increased the Ce^{3+} concentrations which followed the order of CeO_2/NT-TiO_2@0.1 > CeO_2/NR-TiO_2@0.1 > CeO_2/NP-TiO_2@0.1 > CeO_2/NW-TiO_2@0.1. The combination of TiO_2 nanotube with CeO_2 presented the highest concentration of Ce^{3+}, which was because CeO_2 particles were highly dispersed on TiO_2 nanotubes with increased interfacial hybridization, leading to the stabilization of more Ce^{3+}.[36−38] However, correlated with their peroxidase-like activities, it was surprisingly found that a high rather than a low Ce^{3+}/Ce^{4+} ratio facilitated the reaction process and that the activity was positively relevant to the Ce^{3+}/Ce^{4+} ratio. In addition, surface H_2O_2 and PO_4^{2-} treatments were adopted to diminish the Ce^{3+} species of CeO_2/NT-TiO_2@0.1.[28,29] After H_2O_2 and PO_4^{2-} treatments, the concentrations of Ce^{3+} decreased to 48.4% and 43.7% (Table 3), respectively. Meanwhile, their peroxidase-like activities both decreased and a lower activity was found for PO_4^{2-} treated CeO_2/NT-TiO_2@0.1 with a lower Ce^{3+}/Ce^{4+} ratio (Figure 8). These results suggested that the catalytic

Table 3. Concentration of Ce^{3+} and Ce^{4+} Calculated by XPS Spectra

catalyst	concentration of Ce^{3+} (%)[a]	concentration of Ce^{4+} (%)[b]
CeO_2	28.1	71.9
CeO_2/NT-TiO_2@0.1	57.6	42.4
CeO_2/NW-TiO_2@0.1	29.8	70.2
CeO_2/NR-TiO_2@0.1	36.3	63.7
CeO_2/NP-TiO_2@0.1	31.2	68.8
CeO_2/NT-TiO_2@0.1 treated by H_2O_2	48.4	51.6
CeO_2/NT-TiO_2@0.1 treated by PO_4^{2-}	43.7	56.3

[a]Relative concentration of $Ce^{3+} = [A_{Ce^{3+}}/(A_{Ce^{3+}} + A_{Ce^{4+}})] \times 100\%$. [b]Relative concentration of $Ce^{4+} = [A_{Ce^{4+}}/(A_{Ce^{3+}} + A_{Ce^{4+}})] \times 100\%$; $A_{Ce^{3+}}$ and $A_{Ce^{4+}}$ are the total area of peaks assigned to Ce^{3+} and Ce^{4+}, respectively.

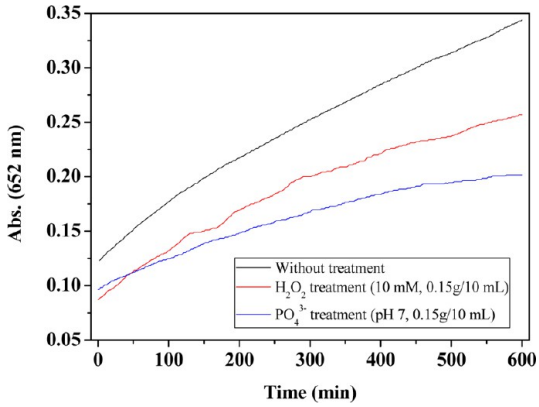

Figure 8. Time-dependent absorbance changes at 652 nm of TMB for CeO_2/NT-TiO_2@0.1 under different surface treatments. Experimental section: To acquire CeO_2/NT-TiO_2@0.1 treated with phosphate buffered saline or H_2O_2, 0.15 g of CeO_2/NT-TiO_2@0.1 was incubated in 10 mL of pH 7 phosphate buffered saline (PBS) and 10 mM H_2O_2 aqueous solution under stirring for 72 and 24 h, respectively. After that, the CeO_2/NT-TiO_2@0.1 was separated, washed, and dried.

reaction of the CeO_2/NT-TiO_2@0.1 + TMB + H_2O_2 system did not follow the reported mechanism,[28,30−32,38] and it was mostly centered on the surface Ce^{3+} sites and more Ce^{3+} sites were favored for activity.[50−52] Raman spectra of NT-TiO_2 (Figure 9a), NP-CeO_2 (Figure 9b), and CeO_2/NT-TiO_2@0.1 (Figure 9c) with and without H_2O_2 treatment were investigated. The Raman bands at 127, 153, 201, 253, 414, 473, 519, and 640 cm^{-1} in NT-TiO_2 were assigned to the anatase structure (Figure 9a).[53] NP-CeO_2 displayed a strong band at 463 cm^{-1} (Figure 9b), which had been assigned to the F_{2g} vibration mode of the O atoms around each Ce^{4+} cation.[54] The band at 593 cm^{-1} was known to be associated with the oxygen vacancies.[55] CeO_2/NT-TiO_2@0.1 showed similar Raman bands at 153, 201, 253, 414, 473, 519, and 640 cm^{-1} as NT-TiO_2, and no obvious Raman bands for CeO_2 were observed (Figure 9c) due to the fact that CeO_2 was well dispersed on the NT-TiO_2 surface and the signals for CeO_2 were masked by those of NT-TiO_2. For the NT-TiO_2 treated

DOI: 10.1021/acsami.5b00023
ACS Appl. Mater. Interfaces 2015, 7, 6451−6461

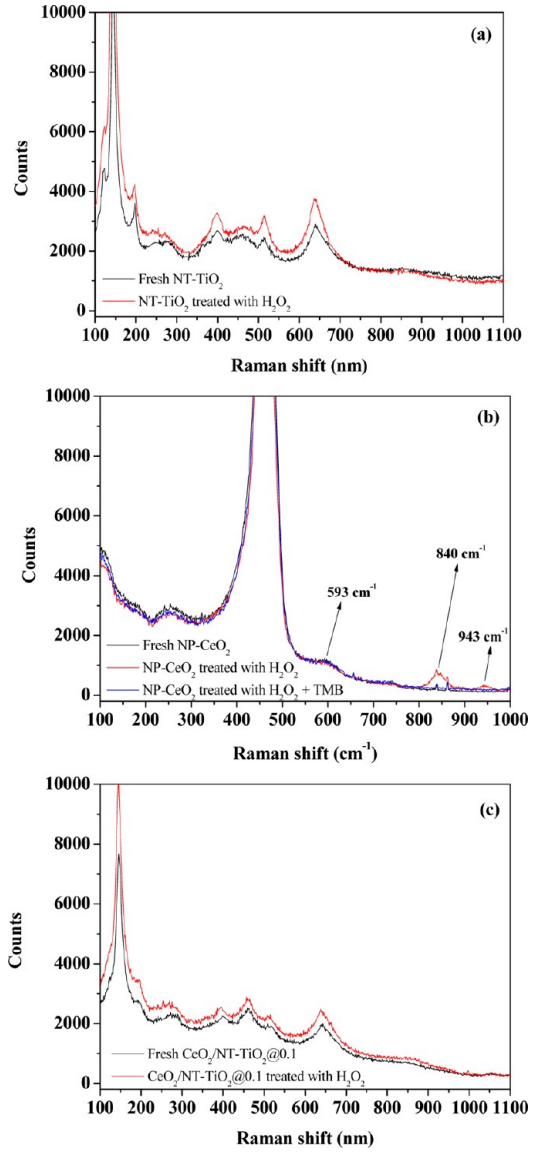

Figure 9. Raman spectra of NT-TiO_2 (a), NP-CeO_2 (b), and CeO_2/NT-TiO_2@0.1 (c) with and without H_2O_2 treatment. Experimental section: 0.1 mL of H_2O_2 (25−28 wt %) was added into 1 g/L aqueous suspension of NT-TiO_2, NP-CeO_2, and CeO_2/NT-TiO_2@0.1 (50 mL) and then stirred vigorously for 1 h. After that, NT-TiO_2, NP-CeO_2, and CeO_2/NT-TiO_2@0.1 powders were collected by centrifugation and washed thoroughly with H_2O to obtain samples with H_2O_2 treatment.

with H_2O_2, no obvious difference of Raman bands was found. Also, the same phenomenon was observed for CeO_2/NT-TiO_2@0.1 with and without H_2O_2 treatment. Due to no obvious Raman bands for surface CeO_2 active sites in the CeO_2/NT-TiO_2@0.1 catalyst, this result was inadequate to illustrate the reaction of surface CeO_2 with H_2O_2. Because of the similar preparation of NP-CeO_2 and CeO_2 responsible for catalysis, the NP-CeO_2 was thus applied to investigate indirectly the reaction of surface CeO_2 with H_2O_2 in CeO_2/NT-TiO_2@0.1. In NP-CeO_2, H_2O_2 pretreatment had not obviously decreased the Raman band at 593 cm^{-1}, which suggested that the oxygen vacancies did not disappear in the presence of H_2O_2. Two new bands appeared at 840 and 943 cm^{-1} in the presence of H_2O_2, which were characteristic features of surface bidentate chelating peroxide and nonplanar bridging peroxide species, respectively.[56−58] When TMB was added, these peaks disappeared and the blue color of TMB oxidation product appeared, which indicated that the formed surface peroxides were responsible for the oxidation of TMB. On the basis of these results, it was concluded that the first interaction of surface CeO_2 with H_2O_2 chemically changed the surface state of CeO_2 by transforming Ce^{3+} sites into surface peroxide species which resulted in adsorbed TMB oxidation in the CeO_2/NT-TiO_2@0.1 + TMB + H_2O_2 system,[50−52] as shown in Figure 10. CeO_2/NT-TiO_2@0.1 had the highest

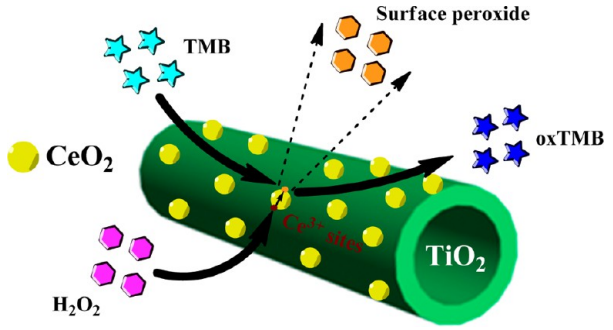

Figure 10. Schematic presentation for TMB oxidation in the presence of H_2O_2 over CeO_2/NT-TiO_2@0.1.

concentration of Ce^{3+} thus leading to the best peroxidase-like activity. At the same time, the highly dispersed CeO_2 and large BET surface area and pore volume in CeO_2/NT-TiO_2@0.1 probably helped to increase the contact of Ce^{3+} active sites with H_2O_2.[59−61]

H_2O_2 and Glucose Detection Using CeO_2/NT-TiO_2@0.1. H_2O_2 and glucose detections are two common analyses in biomedicine diagnosis.[62] On the basis of the intrinsic peroxidase-like property of CeO_2/NT-TiO_2@0.1, we developed a simple colorimetric method to detect H_2O_2 and glucose contents using the catalyzed color reaction. As the absorbance of oxidized TMB was in proportion to H_2O_2 concentration, it was a facile approach to detect H_2O_2 at 652 nm only using a spectrophotometer. Figure 11a showed a typical H_2O_2 concentration response curve where as low as 3.2 μM H_2O_2 could be detected with a linear range from 5 to 100 μM. For glucose detection, glucose oxidase catalyzed the oxidation of glucose to produce gluconic acid and hydrogen peroxide in the presence of oxygen. Subsequently, the formed hydrogen peroxide was catalyzed by CeO_2/NT-TiO_2@0.1 and then reacted with TMB, resulting in the development of a blue color. Therefore, the color change from the converted TMB was employed to indirectly measure glucose content. Results of glucose detection were presented in Figure 11b. As illustrated, the absorbance was linearly correlated to glucose concentration from 0.01 to 0.5 mM with a detection limit of 6.1 μM. In addition, the glucose contents in human serums (provided by the Hospital of Jiangnan University) were detected by this method, and the results were summarized in Table 4. Obviously, the concentrations of glucose examined by our method were quite close to those determined by the Automatic Biochemical Instrument (FH-400) in the Hospital of Jiangnan University. These results indicated that this method can be potentially applied to the determination of glucose content in human serums.

DOI: 10.1021/acsami.5b00023
ACS Appl. Mater. Interfaces 2015, 7, 6451−6461

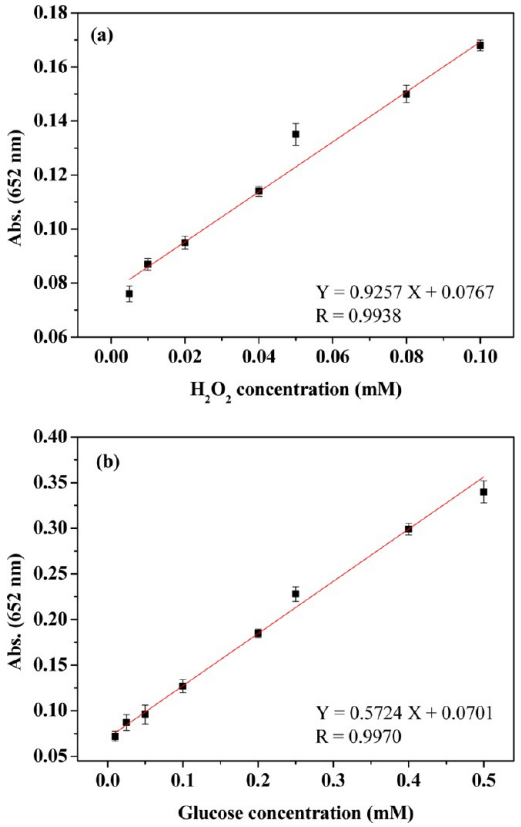

Figure 11. Linear calibration plot for H_2O_2 using CeO_2/NT-TiO_2@0.1 nanocomposite as an artificial enzyme (a); linear calibration plot for glucose detection using GO_x and CeO_2/NT-TiO_2@0.1 nanocomposite (b). Error bars shown represent the standard error derived from three repeated measurements. The limit of detect (LOD) was calculated by the formulation of "LOD = 3S/K", where S was the standard deviation of absorbance for blank sample and K was the slope of the calibration curve.

Table 4. Determination of Glucose Content in Human Serum Samples

sample	content determined by the hospital (mM)	content determined by this colorimetric method (mM)	relative error (%)
1	4.14	4.20	1.45
2	4.56	4.62	1.10
3	5.02	5.09	1.39

CONCLUSIONS

In conclusion, we have demonstrated that CeO_2/NT-TiO_2 nanocomposites possess intrinsic peroxidase-like activity. When the molar ratio of Ce/Ti was 0.1, the best peroxidase-like activity was obtained, which was much higher than comparative CeO_2/NW-TiO_2, CeO_2/NR-TiO_2, and CeO_2/NP-TiO_2 nanocomposites with similar molar ratio of Ce/Ti. The presence of the TiO_2 nanotube support significantly enhanced the dispersion of surface CeO_2 as well as the surface area and pore volume. Additionally, the CeO_2/NT-TiO_2@0.1 nanocomposite exhibited higher affinity to H_2O_2 and TMB than other nanomaterial based peroxidase mimics. Ce^{3+} sites were confirmed as the catalytic active sites for the catalytic reaction. The first interaction of surface CeO_2 with H_2O_2 chemically changed the surface oxidation state of CeO_2 by transforming Ce^{3+} species into surface peroxide species that caused adsorbed TMB oxidation. Compared with CeO_2/NW-TiO_2, CeO_2/NR-TiO_2, and CeO_2/NP-TiO_2, the combination of TiO_2 nanotube with CeO_2 presented the highest concentration of Ce^{3+} thus leading to the best peroxidase-like activity. Moreover, we constructed a simple and sensitive colorimetric assay to detect H_2O_2 and glucose. This study would be significant to propel the development of novel peroxidase mimics materials as well as to provide a deep insight into the correlation between catalyst structure and peroxidase-like activity, catalytic kinetics, and the mechanism. The highly dispersed CeO_2 on the TiO_2 nanotube is expected to be useful not only in the field of peroxidase mimic but also in other promising applications such as a catalytic material.

ASSOCIATED CONTENT

Supporting Information

Table S1: Comparison of the apparent Michaelis–Menten constant (K_m) and maximal velocity (V_m) of the CeO_2/NT-TiO_2@0.1 and other peroxidase mimics. Figure S1: SEM images of TiO_2, CeO_2, and CeO_2/NT-TiO_2. Figure S2: Time-dependent absorbance changes at 652 nm of TMB under different conditions. Figure S3: Dependence of the peroxidase-like activity on TMB concentration. Figure S4: UV–vis spectra of TMB solution with different H_2O_2 concentration after 10 min. Figure S5: Dependence of the peroxidase-like activity on (a) pH and (b) temperature. Figure S6: UV–vis spectra of TMB incubating with the supernatant solution. Figure S7: High-resolution Ce 3d XPS spectra of pure CeO_2. This material is available free of charge via the Internet at http://pubs.acs.org/.

AUTHOR INFORMATION

Corresponding Authors

*Fax: +86 510 85917763. E-mail: dongym@jiangnan.edu.cn.
*Fax: +86 510 85917763. E-mail: ppjiang@jiangnan.edu.cn.

Notes

The authors declare no competing financial interest.

ACKNOWLEDGMENTS

The authors gratefully acknowledge the support from the National Natural Science Foundation of China (Nos. 20903048 and 21275065), the Fundamental Research Funds for the Central Universities (JUSRP51314B, JUSRP13015), the Postgraduate Innovation Project of Jiangsu Province (CXZZ13-0743), and MOE & SAFEA for the 111 Project (B13025).

REFERENCES

(1) Chen, Y.; Cao, H.; Shi, W.; Liu, H.; Huang, Y. Fe-Co Bimetallic Alloy Nanoparticles as a Highly Active Peroxidase Mimetic and Its Application in Biosensing. *Chem. Commun.* **2013**, *49*, 5013–5015.
(2) Qiao, F.; Chen, L.; Li, X.; Li, L.; Ai, S. Peroxidase-Like Activity of Manganese Selenide Nanoparticles and Its Analytical Application for Visual Detection of Hydrogen Peroxide and Glucose. *Sens. Actuators, B* **2014**, *193*, 255–262.
(3) Zhou, Y. T.; He, W.; Wamer, W. G.; Hu, X.; Wu, X.; Martin, Y.; Yin, J. J. Enzyme-Mimetic Effects of Gold@Platinum Nanorods on the Antioxidant Activity of Ascorbic Acid. *Nanoscale* **2013**, *5*, 1583–1591.
(4) Gao, Z.; Xu, M.; Hou, L.; Chen, G.; Tang, D. Irregular-Shaped Platinum Nanoparticles as Peroxidase Mimics for Highly Efficient Colorimetric Immunoassay. *Anal. Chim. Acta* **2013**, *776*, 79–86.
(5) Wang, G.; Xu, X.; Qiu, L.; Dong, Y.; Li, Z.; Zhang, C. Dual Responsive Enzyme Mimicking Activity of AgX (X = Cl, Br, I) Nanoparticles and Its Application for Cancer Cell Detection. *ACS Appl. Mater. Interfaces* **2014**, *6*, 6434–6442.

DOI: 10.1021/acsami.5b00023
ACS Appl. Mater. Interfaces 2015, 7, 6451–6461

(6) Cai, K.; Lv, Z.; Chen, K.; Huang, L.; Wang, J.; Shao, F.; Wang, Y.; Han, H. Aqueous Synthesis of Porous Platinum Nanotubes at Room Temperature and Their Intrinsic Peroxidase-Like Activity. *Chem. Commun.* **2013**, *49*, 6024−6026.
(7) Shi, W.; Zhang, X.; He, S.; Huang, Y. $CoFe_2O_4$ Magnetic Nanoparticles as a Peroxidase Mimic Mediated Chemiluminescence for Hydrogen Peroxide and Glucose. *Chem. Commun.* **2011**, *47*, 10785−10787.
(8) Jv, Y.; Li, B.; Cao, R. Positively-Charged Gold Nanoparticles as Peroxidiase Mimic and Their Application in Hydrogen Peroxide and Glucose Detection. *Chem. Commun.* **2010**, *46*, 8017−8019.
(9) Lien, C. W.; Huang, C. C.; Chang, H. T. Peroxidase-Mimic Bismuth-Gold Nanoparticles for Determining the Activity of Thrombin and Drug Screening. *Chem. Commun.* **2012**, *48*, 7952−7954.
(10) Hu, X.; Saran, A.; Hou, S.; Wen, T.; Ji, Y.; Liu, W.; Zhang, H.; He, W.; Yin, J. J.; Wu, X. Au@PtAg Core/Shell Nanorods: Tailoring Enzyme-Like Activities via Alloying. *RSC Adv.* **2013**, *3*, 6095−6105.
(11) Shi, W.; Wang, Q.; Long, Y.; Cheng, Z.; Chen, S.; Zheng, H.; Huang, Y. Carbon Nanodots as Peroxidase Mimetics and Their Applications to Glucose Detection. *Chem. Commun.* **2011**, *47*, 6695−6697.
(12) Song, Y.; Qu, K.; Zhao, C.; Ren, J.; Qu, X. Graphene Oxide: Intrinsic Peroxidase Catalytic Activity and Its Application to Glucose Detection. *Adv. Mater.* **2010**, *22*, 2206−2210.
(13) Liu, M.; Zhao, H.; Chen, S.; Yu, H.; Quan, X. Interface Engineering Catalytic Graphene for Smart Colorimetric Biosensing. *ACS Nano* **2012**, *6*, 3142−3151.
(14) Liu, M.; Chen, S.; Yu, H.; Quan, X. Stimuli-Responsive Peroxidase Mimicking at a Smart Graphene Interface. *Chem. Commun.* **2012**, *48*, 7055−7057.
(15) Tao, Y.; Lin, Y.; Huang, Z.; Ren, J.; Qu, X. Incorporating Graphene Oxide and Gold Nanoclusters: A Synergistic Catalyst with Surprisingly High Peroxidase-Like Activity Over a Broad pH Range and its Application for Cancer Cell Detection. *Adv. Mater.* **2013**, *25*, 2594−2599.
(16) Chen, H.; Li, Y.; Zhang, F.; Zhang, G.; Fan, X. Graphene Supported Au-Pd Bimetallic Nanoparticles with Core-Shell Structures and Superior Peroxidase-Like activities. *J. Mater. Chem.* **2011**, *21*, 17658−17661.
(17) Zhang, Y.; Xu, C.; Li, B.; Li, Y. In Situ Growth of Positively-Charged Gold Nanoparticles on Single-Walled Carbon Nanotubes as a Highly Active Peroxidase Mimetic and Its Application in Biosensing. *Biosens. Bioelectron.* **2013**, *43*, 205−210.
(18) Yu, F.; Huang, Y.; Cole, A. J.; Yang, V. C. The Artificial Peroxidase Activity of Magnetic Iron Oxide Nanoparticles and Its Application to Glucose Detection. *Biomaterials* **2009**, *30*, 4716−4722.
(19) Mu, J.; Wang, Y.; Zhao, M.; Zhang, L. Intrinsic Peroxidase-Like Activity and Catalase-Like Activity of Co_3O_4 Nanoparticles. *Chem. Commun.* **2012**, *48*, 2540−2542.
(20) Hu, L.; Yuan, Y.; Zhang, L.; Zhao, J.; Majeed, S.; Xu, G. Copper Nanoclusters as Peroxidase Mimetics and Their Applications to H_2O_2 and Glucose Detection. *Anal. Chim. Acta* **2013**, *762*, 83−86.
(21) André, R.; Natálio, F.; Humanes, M.; Leppin, J.; Heinze, K.; Wever, R.; Schröder, H. C.; Müller, W. E. G.; Tremel, W. V_2O_5 Nanowires with an Intrinsic Peroxidase-Like Activity. *Adv. Funct. Mater.* **2011**, *21*, 501−509.
(22) Campbell, C. T.; Peden, C. H. F. Oxygen Vacancies and Catalysis on Ceria Surfaces. *Science* **2005**, *309*, 713−714.
(23) Yu, X.; Kuai, L.; Geng, B. CeO_2/rGO/Pt Sandwich Nanostructure: rGO-Enhanced Electron Transmission between Metal Oxide and Metal Nanoparticles for Anodic Methanol Oxidation of Direct Methanol Fuel Cells. *Nanoscale* **2012**, *4*, 5738−5743.
(24) Lee, Y.; He, G.; Akey, A. J.; Si, R.; Flytzani-Stephanopoulos, M.; Herman, I. P. Raman Analysis of Mode Softening in Nanoparticle $CeO_{2-\delta}$ and Au-$CeO_{2-\delta}$ during CO Oxidation. *J. Am. Chem. Soc.* **2011**, *133*, 12952−12955.
(25) Si, R.; Flytzani-Stephanopoulos, M. Shape and Crystal-Plane Effects of Nanoscale Ceria on the Activity of Au-CeO_2 Catalysts for the Water-Gas Shift Reaction. *Angew. Chem.* **2008**, *120*, 2926−2929.
(26) González-Rovira, L.; Sánchez-Amaya, J. M.; López-Haro, M.; Rio, E.; Hungría, A. B.; Midgley, P.; Calvino, J. J.; Bernal, S.; Botana, F. J. Single-Step Process To Prepare CeO_2 Nanotubes with Improved Catalytic Activity. *Nano Lett.* **2009**, *9*, 1395−1400.
(27) Korsvik, C.; Patil, S.; Seal, S.; Self, W. T. Superoxide Dismutase Mimetic Properties Exhibited by Vacancy Engineered Ceria Nanoparticles. *Chem. Commun.* **2007**, 1056−1058.
(28) Pirmohamed, T.; Dowding, J. M.; Singh, S.; Wasserman, B.; Heckert, E.; Karakoti, A. S.; King, J. E. S.; Seal, S.; Self, W. T. Nanoceria Exhibit Redox State-Dependent Catalase Mimetic Activity. *Chem. Commun.* **2010**, *46*, 2736−2738.
(29) Heckert, E. G.; Karakoti, A. S.; Seal, S.; Self, W. T. The Role of Cerium Redox State in the SOD Mimetic Activity of Nanoceria. *Biomaterials* **2008**, *29*, 2705−2709.
(30) Celardo, I.; Pedersen, J. Z.; Traversa, E.; Ghibelli, L. Pharmacological Potential of Cerium Oxide Nanoparticles. *Nanoscale* **2011**, *3*, 1411−1420.
(31) Celardo, I.; Nicola, M. D.; Mandoli, C.; Pedersen, J. Z.; Traversa, E.; Ghibelli, L. Ce^{3+} Ions Determine Redox Dependent Anti-Apoptotic Effect of Cerium Oxide Nanoparticles. *ACS Nano* **2011**, *5*, 4537−4549.
(32) Walkey, C.; Das, S.; Seal, S.; Erlichman, J.; Heckman, K.; Ghibelli, L.; Traversa, E.; McGinnis, J. F.; Self, W. T. Catalytic Properties and Biomedical Applications of Cerium Oxide Nanoparticles. *Environ. Sci.: Nano* **2015**, DOI: 10.1039/C4EN00138A.
(33) Zhou, G.; Barrio, L.; Agnoli, S.; Senanayake, S. D.; Evans, J.; Kubacka, A.; Estrella, M.; Hanson, J. C.; Martinez-Arias, A.; Fernandez-Garcia, M.; Rodriguez, J. A. High Activity of $Ce_{1-x}Ni_xO_{2-y}$ for H_2 Production through Ethanol Steam Reforming: Tuning Catalytic Performance through Metal-Oxide Interactions. *Angew. Chem., Int. Ed.* **2010**, *49*, 9680−9684.
(34) Gionco, C.; Paganini, M. C.; Agnoli, S.; Reeder, A. E.; Giamello, E. Structural and Spectroscopic Characterization of CeO_2-TiO_2 Mixed Oxides. *J. Mater. Chem. A* **2013**, *1*, 10918−10926.
(35) Chen, L.; Si, Z.; Wu, X.; Wenig. DRIFT Study of CuO-CeO_2-TiO_2 Mixed Oxides for NO_x Reduction with NH_3 at Low Temperatures. *ACS Appl. Mater. Interfaces* **2014**, *6*, 8134−8145.
(36) Graciani, J.; Plata, J. J.; Sanz, J. F.; Liu, P.; Rodriguez, J. A. A Theoretical Insight into the Catalytic Effect of a Mixed-Metal Oxide at the Nanometer Level: The Case of the Highly Active Metal/CeO_x/TiO_2(110) Catalysts. *J. Chem. Phys.* **2010**, *132*, 104703.
(37) Agnoli, S.; Reeder, A. E.; Senanayake, S. D.; Hrbek, J.; Rodriguez, J. A. Structure and Special Chemical Reactivity of Interface Stabilized Cerium Oxide Nanolayers on TiO_2(110). *Nanoscale* **2014**, *6*, 800−810.
(38) Artiglia, L.; Agnoli, S.; Paganini, M. C.; Cattelan, M.; Granozzi, G. TiO_2@CeO_x Core-Shell Nanoparticles as Artificial Enzymes with Peroxidase-Like Activity. *ACS Appl. Mater. Interfaces* **2014**, *6*, 20130−20136.
(39) Song, Y.; Gao, Z.; Wang, J.; Xia, X.; Lynch, R. Multistage Coloring Electrochromic Device Based on TiO_2 Nanotube Arrays Modified with WO_3 Nanoparticles. *Adv. Funct. Mater.* **2011**, *21*, 1941−1946.
(40) Song, Y.; Gao, Z.; Lee, K.; Schmuki, P. A Self-Cleaning Nonenzymatic Glucose Detection System Based on Titania Nanotube Arrays Modified with Platinum Nanoparticles. *Electrochem. Commun.* **2011**, *13*, 1217−1220.
(41) Gao, Z.; Han, Y.; Li, Y.; Yang, M.; Song, Y. Photocatalytic Synthesis and Synergistic Effect of Prussian Blue-Decorated Au Nanoparticles/TiO_2 Nanotube Arrays for H_2O_2 Amperometric Sensing. *Electrochim. Acta* **2014**, *125*, 530−535.
(42) Cortes-Jácome, M. A.; Morales, M.; Chavez, C. A.; Ramírez-Verduzco, L. F.; López-Salinas, E.; Toledo-Antonio, J. A. WO_x/TiO_2 Catalysts via Titania Nanotubes for the Oxidation of Dibenzothiophene. *Chem. Mater.* **2007**, *19*, 6605−6614.

DOI: 10.1021/acsami.5b00023
ACS Appl. Mater. Interfaces 2015, 7, 6451−6461

(43) Taai, C.; Teng, H. Regulation of the Physical Chatacteristics of Titania Nanotube Aggregates Synthesized from Hydrothermal Treatment. *Chem. Mater.* **2004**, *16*, 4352−4358.
(44) Song, S.; Liu, Z.; He, Z.; Zhang, A.; Chen, J. Impacts of Morphology and Crystallite Phase of Titanium Oxide on the Catalytic Ozonation of Phenol. *Environ. Sci. Technol.* **2010**, *44*, 3913−3918.
(45) Dutta, A. K.; Maji, S. K.; Srivastava, D. N.; Mondal, A.; Biswas, P.; Paul, P.; Adhikary, B. Synthesis of FeS and FeSe Nanoparticles from a Single Source Precursor: A Study of Their Photocatalytic Activity, Peroxidase-Like Behavior, and Electrochemical Sensing of H_2O_2. *ACS Appl. Mater. Interfaces* **2012**, *4*, 1919−1927.
(46) Hans, L.; Dean, B. The Determination of Enzyme Dissociation Constants. *J. Am. Chem. Soc.* **1934**, *56*, 658−666.
(47) Gao, L.; Zhuang, J.; Nie, L.; Zhang, J.; Zhang, Y.; Gu, N.; Wang, T.; Feng, J.; Yang, D.; Perrett, S. Intrinsic Peroxidase-Like Activity of Ferromagnetic Nanoparticles. *Nat. Nanotechnol.* **2007**, *2*, 577−583.
(48) Bêche, E.; Charvin, P.; Perarnau, D.; Abanades, S.; Flamant, G. Ce 3d XPS Investigation of Cerium Oxides and Mixed Cerium Oxide ($Ce_xTi_yO_z$). *Surf. Interface Anal.* **2008**, *40*, 264−267.
(49) Natile, M. M.; Glisenti, A. CoO_x/CeO_2 Nanocomposite Powders: Synthesis, Characterization, and Reactivity. *Chem. Mater.* **2005**, *17*, 3403−3414.
(50) Cai, W.; Chen, F.; Shen, X.; Chen, L.; Zhang, J. Enhanced Catalytic Degradation of AO7 in the CeO_2-H_2O_2 System with Fe^{3+} Doping. *Appl. Catal., B* **2010**, *101*, 160−168.
(51) Chen, F.; Shen, X.; Wang, Y.; Zhang, J. CeO_2/H_2O_2 System Catalytic Oxidation Mechanism Study via a Kinetics Investigation to the Degradation of Acid Orange 7. *Appl. Catal., B* **2012**, *121−122*, 223−229.
(52) Ji, P.; Wang, L.; Chen, F.; Zhang, J. Ce^{3+}-Centric Organic Pollutant Elimination by CeO_2 in the Presence of H_2O_2. *ChemCatChem* **2010**, *2*, 1552−1554.
(53) Li, Z.; Wnetrzak, R.; Kwapinski, W.; Leahy, J. J. Synthesis and Characterization of Sulfated TiO_2 Nanorods and ZrO_2/TiO_2 Nanocomposites for the Esterification of Biobased Organic Acid. *ACS Appl. Mater. Interfaces* **2012**, *4*, 4499−4505.
(54) Twu, J.; Chuang, C. J.; Chang, K.; Yang, C. H.; Chen, K. H. Raman Spectroscopic Studies on the Sulfation of Cerium Oxide. *Appl. Catal., B* **1997**, *12*, 309−324.
(55) Spanier, J. E.; Robinson, R. D.; Zhang, F.; Chan, S. W.; Herman, I. P. Size-Dependent Properties of CeO_{2-y} Nanoparticles as Studied by Raman Scattering. *Phys. Rev. B* **2001**, *64*, 245407.
(56) Guzman, J.; Carrettin, S.; Corma, A. Spectroscopic Evidence for the Supply of Reactive Oxygen during CO Oxidation Catalyzed by Gold Supported on Nanocrystalline CeO_2. *J. Am. Chem. Soc.* **2005**, *127*, 3286−3287.
(57) Pushkarev, V. V.; Kovalchuk, V. I.; d'Itri, J. L. Probing Defect Sites on the CeO_2 Surface with Dioxygen. *J. Phys. Chem. B* **2004**, *108*, 5341−5348.
(58) Scholes, F. H.; Hughes, A. E.; Hardin, S. G.; Lynch, P.; Miller, P. R. Influence of Hydrogen Peroxide in the Preparation of Nanocrystalline Ceria. *Chem. Mater.* **2007**, *19*, 2321−2328.
(59) Li, H.; Lu, G.; Dai, Q.; Wang, Y.; Guo, Y.; Guo, Y. Hierarchical Organization and Catalytic Activity of High-Surface-Area Mesoporous Ceria Microspheres Prepared Via Hydrothermal Routes. *ACS Appl. Mater. Interfaces* **2010**, *2*, 836−846.
(60) Yagati, A. K.; Lee, T.; Min, J.; Choi, J.-W. An Enzymatic Biosensor for Hydrogen Peroxide Based on CeO_2 Nanostructure Electrodeposited on ITO Surface. *Biosens. Bioelectron.* **2013**, *47*, 385−390.
(61) Shan, W.; Liu, F.; He, H.; Shi, X.; Zhang, C. An Environmentally-Benign CeO_2-TiO_2 Catalyst for the Selective Catalytic Reduction of NO_x with NH_3 in Simulated Diesel Exhaust. *Catal. Today* **2012**, *184*, 160−165.
(62) Zhou, L.; Kuai, L.; Li, W.; Geng, B. Ion-Exchange Route to Au-Cu_xOS Yolk-Shell Nanostructures with Porous Shells and Their Ultrasensitive H_2O_2 Detection. *ACS Appl. Mater. Interfaces* **2012**, *4*, 6463−6467.

DOI: 10.1021/acsami.5b00023
ACS Appl. Mater. Interfaces 2015, 7, 6451−6461